Materials Science & Engineering A 771 (2020) 138578

Contents lists available at ScienceDirect

Materials Science & Engineering A

journal homepage: http://www.elsevier.com/locate/msea

Effect of post-deformation annealing on the microstructure and micro-mechanical behavior of Zn–Mg hybrids processed by High-Pressure Torsion

David Hernández-Escobar [a,*], Joshua Marcus [a], Jae-Kyung Han [b], Raymond R. Unocic [c], Megumi Kawasaki [b], Carl J. Boehlert [a]

[a] Department of Chemical Engineering and Materials Science, Michigan State University, East Lansing, MI, 48824, USA
[b] School of Mechanical, Industrial and Manufacturing Engineering, Oregon State University, Corvallis, OR, 97331, USA
[c] Center for Nanophase Materials Sciences, Oak Ridge National Laboratory, Oak Ridge, TN, 37831, USA

ARTICLE INFO

Keywords:
High-pressure torsion
Hybrid
Intermetallic
Nanoindentation
Zn–Mg

ABSTRACT

Heterostructured metals have attracted increasing interest because of their unique capability to overcome the strength-ductility tradeoff typically observed in engineering materials. Here, a new strategy for synthesizing heterostructured Zn–Mg hybrids is proposed via high-pressure torsion (HPT) followed by post-deformation annealing (PDA). Experimental results indicate a transition from a relatively homogenous nanograined structure after HPT, to a heterogeneous microstructure, containing a distribution of Mg_2Zn_{11} and $MgZn_2$ intermetallic nanoprecipitates, upon subsequent PDA. This led to a simultaneous increase in hardness and strain rate sensitivity. The observed three-regime strain hardening behavior was suggested to be due to the activation of multiple strengthening mechanisms, including grain refinement, in-situ precipitation, and back-stress strengthening associated with geometrically necessary dislocations. Thus, the mechanical response of Zn–Mg hybrids may be tailored to obtain the desired response for task-specific applications.

1. Introduction

The processing of Zn-based alloys able to satisfy the demanding requirements of absorbable medical devices is still an open challenge. Bioabsorbable metals should simultaneously fulfill the three following conditions: have an adequate combination of mechanical properties (i.e. tensile strength, elongation-to-failure (ε_f)), show acceptable biocompatibility, and possess a corrosion rate matching that of the healing tissue. The first attempts to develop absorbable metal implants were focused on Mg-based and Fe-based alloys, which generally showed a good combination of mechanical properties, however their corrosion kinetics were too rapid or too slow, respectively [1,2]. In the last few years, Zn has emerged as a potential candidate for the next generation of temporary implant applications due to its similar corrosion behavior in physiological conditions to that of the tissue-healing processes [3,4]. Moreover, both *in-vitro* and *in-vivo* experiments have shown that Zn-based implants exhibit outstanding biocompatibility in vascular and bone tissues [5,6].

Despite having adequate corrosion properties and biocompatibility, the low strength of Zn is not suitable for load-bearing implantable devices. This triggered the investigation of adding different biocompatible alloying elements (i.e. Mg, Ca, Sr), as well as using plastic deformation techniques that would equip Zn-based alloys with a refined microstructure and the associated enhanced strength. Zn–Mg alloys obtained through conventional thermomechanical processes, such as rolling or extrusion, have demonstrated a significant increase in tensile strength and hardness compared to pure Zn [7]. However, this often results in a corresponding reduction of the ε_f, as a consequence of the strength-ductility tradeoff generally observed in engineering materials. Unlike conventional deformation processes, severe plastic deformation (SPD) techniques have the ability to produce ultrafine-grained microstructures, which have been associated with a balance of high strength and adequate ε_f values, for a wide range of metals and alloys [8–10]. High-pressure torsion (HPT) is one of the most attractive SPD techniques in terms of producing true nanostructures in bulk materials [11]. However, the strengthening associated with grain refinement is limited by a steady-state regime reached at high strain values, i.e. 8–10 effective strain [12]. Thereby, grain size saturation limits the strength increase

* Corresponding author. 428 S Shaw Lane, 2100, East Lansing, MI, 48824, USA.
E-mail address: herna437@egr.msu.edu (D. Hernández-Escobar).

https://doi.org/10.1016/j.msea.2019.138578
Received 3 October 2019; Received in revised form 17 October 2019; Accepted 19 October 2019
Available online 22 October 2019
0921-5093/

when processing metallic alloys with microstructural homogeneity. Consequently, an alternative HPT approach, able to promote solid-state reactions through direct diffusion bonding at room temperature (RT), has been investigated for synthesizing metal hybrids (i.e. Al-Cu [13,14], Al-Mg [15,16], Al-Fe [17], Al-Ti [17], Cu-Ta [18] and Zn–Mg [19]).

Metal systems containing Al are commonly ruled out in the biomedical field, as the presence of Al ions in humans has been associated with the development of neurodegenerative disorders, such as dementia [20] and Alzheimer's disease [21]. Thus, from a health safety perspective, the Zn–Mg system becomes the most attractive candidate among the HPT hybrids studied so far. A previous work [19] demonstrated the successful bonding of Zn–Mg hybrids through HPT with minimal segregation, where ultrafine-grained microstructures containing intermetallic compounds contributed to exceptional hardening. Moreover, electrochemical studies revealed that the corrosion resistance and electrochemical kinetics were similar to that of Zn [19]. This study confirmed the feasibility of HPT processing at RT for joining Zn and Mg in order to obtain metal hybrids with enhanced hardness.

The present work aims to investigate the effect of post-deformation annealing (PDA) on the microstructural evolution and hardness of Zn–Mg hybrids processed by HPT. It is shown that heterogeneous nanostructured Zn–Mg hybrids can benefit from a short PDA treatment to simultaneously enhance both the hardness and strain rate sensitivity. Microscopic examination indicated a transition from a relatively homogenous nanograined microstructure after HPT processing, to a heterogeneous microstructure consisting of nanosized clusters within a submicron grained matrix after HPT + PDA. The variation in size and distribution of the grains and the HPT-induced intermetallic particles contributed to this unusual response. HPT followed by PDA can not only make Zn–Mg hybrids attractive for absorbable biomedical applications [22], but also guide researchers towards novel material design strategies aimed at defying the so-called "Paradox of strength and ductility" [23].

2. Experimental material and methods

2.1. Sample preparation

A series of pure Zn and pure Mg disks, having a 10 mm diameter, were prepared for HPT processing. Each HPT hybrid specimen consisted of a set of three disks stacked on top of each other in the order of Zn/Mg/Zn. The thickness of the top and bottom Zn disks was 0.665 mm, whereas the thickness of the center Mg disk was 0.169 mm, such that the final bulk composition of the resulting HPT hybrid samples was anticipated as Zn–3Mg (wt. %). The three disks where diffusion-bonded using a quasi-constrained HPT facility into a single hybrid of approximately 0.85 mm final thickness. Processing was conducted at RT under an applied pressure of 6 GPa, at a constant rotational speed of 1 rpm, for a total number of 1, 5, 15 and 30 turns. Some samples after HPT for 30 turns were then subjected to a PDA treatment of 200 °C for 1 h in a vacuum tube furnace followed by air cooling. It should be noted that the temperature rise was monitored during HPT processing, obtaining a maximum temperature below 50 °C, which is considered insufficient to have any significant effect in the microstructural evolutions reported, in agreement with a recent report [24]. Further details regarding the experimental set up and metallographic preparation can be found elsewhere [19].

2.2. Microstructural characterization

Scanning electron microscopy (SEM) was performed using a Tescan Mira3 FEG-SEM. Backscattered electron (BSE) imaging was performed at the periphery (less than 1 mm away from the disk edge) of the cross-section in the HPT hybrid samples. All the SEM images presented were taken in the thickness-radial plane, as illustrated schematically in Fig. 1. An accelerating voltage of 20 kV and 6 mm working distance were used for acquiring images, from which the average grain size was estimated following the linear intercept method.

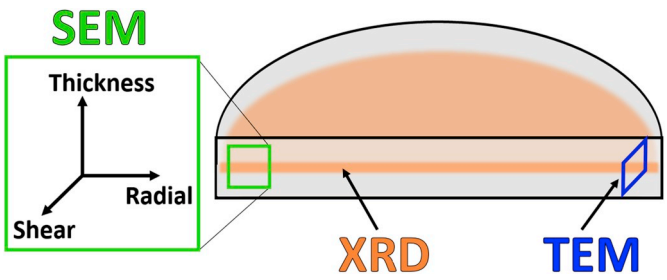

Fig. 1. Schematic representation of the analysis planes investigated in the Zn–3Mg HPT hybrid disks through scanning electron microscopy (SEM), transmission electron microscopy (TEM), and x-ray diffraction (XRD). SEM images were taken at the thickness-radial plane. TEM images were taken at the thickness-shear plane. XRD data was collected from the shear-radial plane.

Transmission electron microscopy (TEM) and scanning-transmission electron microscopy (STEM) was performed using a FEI Titan aberration-corrected TEM/STEM operated at 300 kV. A focused-ion beam (FIB) lift-out technique was conducted in a Hitachi NB5000 FIB-SEM to extract specimens with approximate dimensions of 5×15 µm. All TEM/STEM images were taken in the shear-thickness plane at the periphery of the HPT disks. As observed in Fig. 1, the imaging planes for SEM and TEM/STEM are perpendicular, defining a coordinate system (thickness-radial-shear) which enables a three-dimensional characterization of the microstructure. Phase contrast images, as well as selected area electron diffraction (SAED) patterns were collected in TEM mode, whereas bright field (BF) and high-angle annular dark field (HAADF) images were acquired in STEM mode. High resolution TEM (HRTEM) imaging was also performed, and the corresponding Fast Fourier Transform (FFT) diffractograms were obtained and analyzed using DigitalMicrograph.

X-ray diffraction (XRD) analysis was carried out using a high resolution Rigaku Ultima IV XRD system to assess the microstructural development and phase changes. An accelerating voltage of 44 kV and a beam intensity of 44 mA were selected for data collection within the range $30° < 2\theta < 90°$ using a Cu-Kα radiation in a Bragg-Brentano configuration. A step size of 0.01°/step and a scan speed of 3°/min were used for all the scans. According to the Beer-Lambert law, the X-ray beam penetrates ~0.26 mm deep into the sample with the aforementioned settings. Therefore, the HPT hybrid disks were slightly polished in the thickness direction prior to XRD analysis, in order to investigate the mid-thickness plane depicted in Fig. 1. The PDXL Rigaku Analysis software was used, along with the Inorganic Crystal Structure Database (ICSD), for peak matching in order to identify the phases present.

2.3. Micro-mechanical testing

Vickers microhardness (HV) measurements were taken from the cross-section along the disk diameter of the HPT-processed hybrids using a Clark CM-800AT microhardness tester. HV values were recorded following a rectilinear grid pattern at a uniform incremental spacing of 0.15 mm in the horizontal (radial) and vertical (thickness) directions, with a load of 50 gf and a dwell time of 5 s. The resulting data set was plotted directly (with no averaging nor manipulation) in the form of color-coded contour maps to provide a comparative visual representation of the distribution and evolution of the hardness values across the disk during HPT processing.

Nanoindentation experiments were performed at constant strain rate (CSR) at the mid-thickness plane of the disk periphery of the HPT hybrid samples using a MTS nanoindenter XP with a three-sided pyramidal Berkovich indenter having a centerline-to-face angle of 65.3°. A nanoindentation method, able to perform CSR experiments, was created according to the proportional loading protocol described by Lucas and Oliver [25]. Equation (1) indicates the relationship between $\dot{\varepsilon}_i$, the

indentation strain rate, h, the indentation depth, P, the indentation load, and H, the indentation hardness.

$$\dot{\varepsilon}_i = \frac{\dot{h}}{h} = \frac{1}{2}\cdot\left(\frac{\dot{P}}{P} - \frac{\dot{H}}{H}\right) \approx \frac{1}{2}\frac{\dot{P}}{P} \quad (1)$$

Nanoindentation tests consisted of an initial loading segment at a specific CSR ($\dot{\varepsilon}_i$= 0.0125, 0.025, 0.05, 0.1 s^{-1}) to a prescribed maximum load (P_{max} = 50 mN), which was maintained during a hold segment of 10 s, followed by unloading at the same CSR. The experimental indentation strain rates, $\dot{\varepsilon}_i$, were equivalent to uniaxial strain rates ($\dot{\varepsilon} = 0.01\cdot\dot{\varepsilon}_i$ = $1.25\cdot10^{-4}$, $2.5\cdot10^{-4}$, $5.0\cdot10^{-4}$, and $1.0\cdot10^{-3}$ s^{-1}) as determined from an empirical relationship [26,27]. A rectilinear array of 12 individual measurements was performed for each of the four CSR examined, where a separation of 30 μm between indents, in both the horizontal and vertical directions, was maintained. The initial unloading portion of the resulting load vs. displacement curves was used to compute the values of H at different CSR according to the Oliver-Pharr method [28]. The strain rate sensitivity, m, was determined by Equation (2), which considers the Tabor's empirical relationship [29] where the flow stress, σ_f, is equivalent to $H/3$ for fully plastic deformation at a constant $\dot{\varepsilon}$. The mechanism of plastic deformation can be estimated through the activation volume, V^*, which was calculated from m and H using Equation (3) [30], where k is the Boltzmann's constant and T is the testing temperature.

$$m = \left(\frac{\partial \ln\sigma_f}{\partial \ln\dot{\varepsilon}}\right)_{\varepsilon,T} = \left(\frac{\partial \ln(H/3)}{\partial \ln(0.01\cdot\dot{\varepsilon}_i)}\right)_{\varepsilon,T} \quad (2)$$

$$V^* = \sqrt{3}kT\cdot\left(\frac{\partial \ln\dot{\varepsilon}}{\partial\, \sigma_f}\right) = \sqrt{3}kT\cdot\left(\frac{\partial \ln(0.01\cdot\dot{\varepsilon}_i)}{\partial\, (H/3)}\right) = \frac{3kT\sqrt{3}}{mH} \quad (3)$$

3. Results

3.1. Microstructural and hardness evolution during HPT and subsequent PDA

Fig. 2 (a) shows a series of low magnification BSE−SEM images taken at the cross-sections of the Zn–Mg hybrids after HPT for 1, 5, 15 and 30 turns. In addition, a sample after 30 turns was subjected to a PDA at 200 °C for 1 h, and it is hereafter referred to as 30 turns HPT + PDA. After 1 turn, diffusion bonding was achieved within the Zn/Mg/Zn disk sequence, without evidence of voids or segregation, and the intermediate Mg layer (dark region) was still clearly observed across the disk diameter. After 5 turns, the Mg layer was no longer continuous along the disk diameter. The Mg-rich phase was fragmented into thin regions, especially closer to the disk periphery, $r > 3.0$ mm, where larger plastic deformation occurred. After 15 and 30 turns, the central region of the disks, $r < 2.0$ mm, exhibited finer Mg-rich phases, which were distributed preferentially along the shear direction. Similarly, the microstructure in the outer areas of the disk became more homogenous with increasing number of turns, and there was no macroscopic evidence of Mg-rich phases after 30 turns. A complete mixture of the phases along the cross section of the disk was observed in the 30 turn HPT + PDA material.

The distribution of Vickers microhardness values was examined over the cross-sections of the Zn–Mg HPT hybrids, and the data is presented in the color-coded hardness contour maps shown in Fig. 2 (b). The equivalent hardness values are indicated in the color key on the bottom. The cross-section of the Zn–3Mg hybrid after HPT for 1 turn shows a uniform average microhardness of ~39 HV across the disk, which was very similar to that for pure Zn and pure Mg (37 HV and 35 HV, respectively [31,32]). After 5 turns, higher microhardness values were measured at the peripheral region of the disk, with an average of ~68 HV at $r > 3.0$ mm, whereas an average of ~45 HV was observed at $r < 3.0$ mm. Processing for 15 turns resulted in an increase of the microhardness values to an average of ~116 HV at $r > 2.0$ mm. Similar to that after 5 turns, the central region maintained low hardness, with an average of ~65 HV at $r < 2.0$ mm. Additional processing for 30 turns led not only to a significant increase of the microhardness levels, with an average of ~133 HV across the entire disk, but also to a more homogenous hardness distribution. The maximum hardness values, within the range of ~200–230 HV, were recorded at the peripheral region of the disk, where the Mg-rich phases were no longer distinguishable within the Zn-rich matrix. Overall, there was a symmetric gradient-type evolution of the microhardness with respect to the disk center during HPT processing from 1 to 30 turns, with gradually increasing HV values from the periphery to the center. After PDA, the 30-turns HPT hybrid did not exhibit softening. Instead, the hardness was maintained with an average value of ~139 HV across the disk. Despite this slightly higher average hardness value compared to that before PDA, it was observed that the region at $r < 0.5$ mm showed a decrease in hardness. However, the outermost region of the disk (at $r > 3.0$ mm) after PDA, presented the highest hardness values recorded for this hybrid system, within a range of 210–250 HV.

The microstructures at the periphery of the cross-section of the Zn–3Mg HPT hybrids after 30 turns, and 30 turns + PDA are shown in Fig. 3(a–c) and (d-f), respectively. As shown in Fig. 1, the SEM micrographs presented in Fig. 3 were taken at the same orientation as those in Fig. 2 (a), where the horizontal and vertical directions correspond to the radial and thickness directions, respectively. The ultrafine-grained microstructure after 30 turns, see Fig. 3(a–c), consisted of fairly equiaxed grains with sizes ranging between ~100–200 nm. Vortex-like Mg-rich domains, with an axis perpendicular to the shear direction, often referred as swirls (highlighted with yellow arrows in Fig. 3(a–b)), were

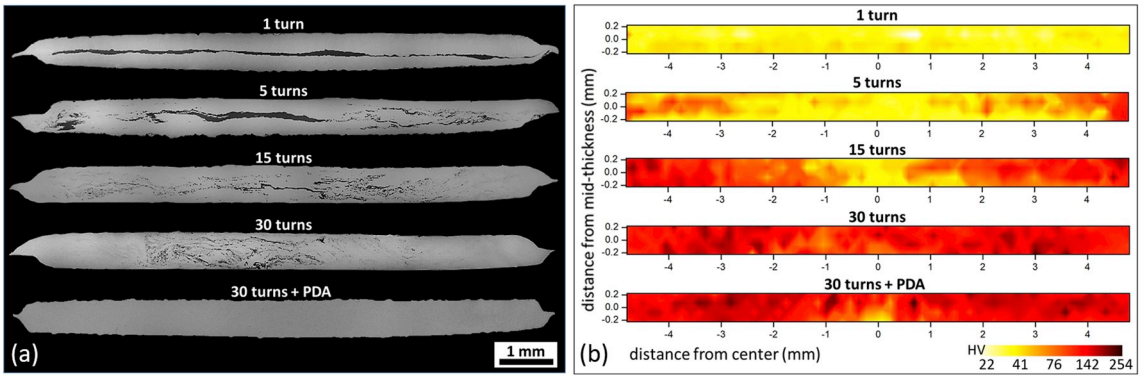

Fig. 2. (a) Cross-sections of the Zn–3Mg hybrids after HPT processing at RT under an applied pressure of 6 GPa and a rotational speed of 1 rpm after 1, 5, 15, 30 turns, and 30 turns + PDA (200 °C, 1 h) and (b) corresponding color-coded Vickers microhardness contour maps. (For interpretation of the references to color in this figure legend, the reader is referred to the Web version of this article.)

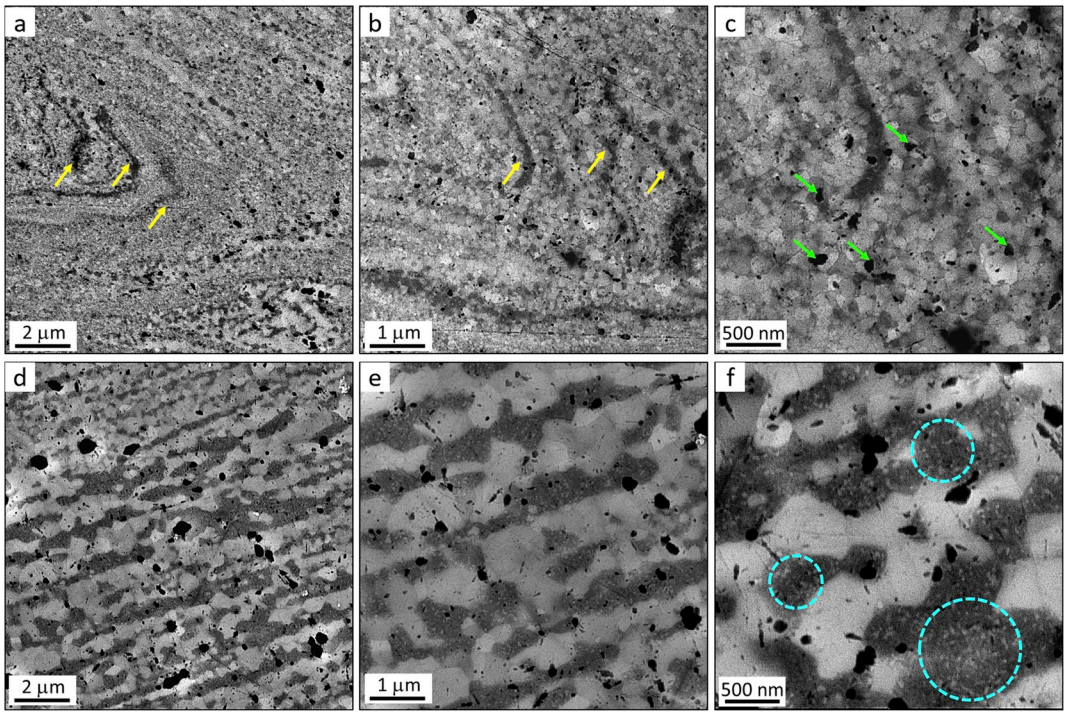

Fig. 3. Representative BSE–SEM micrographs of the Zn–3Mg HPT hybrids at the periphery of the cross-section after (a)–(c) 30 turns, and (d)–(f)30 turns HPT + PDA (200 °C, 1 h) at 20kX, 40kX and 80kX, respectively. Yellow arrows indicate vortex-like Mg-rich domains. Green arrows indicate nanoscale intermetallic precipitates. Blue dashed circles show Mg-rich regions. (For interpretation of the references to color in this figure legend, the reader is referred to the Web version of this article.)

result of local turbulences characteristic of HPT processing [33–36]. Nanosized precipitates (highlighted with green arrows in Fig. 3 (c)), ranging between ~ 20 and 100 nm, with different morphologies were evenly distributed within the Zn-rich matrix. Based on our previous work [19], these are believed to be Zn–Mg intermetallic compounds. After PDA, the microstructure evolved significantly, as observed in Fig. 3 (d–f). The average grain size increased to ~200–1000 nm with an associated spread in the grain size distribution. A multilayered microstructure, reasonably aligned with the shear direction, was evident in Fig. 3 (d). In addition, the complex Mg-rich shearing patterns were no longer present. Moreover, Mg-rich regions, (highlighted with blue dashed circles in Fig. 3 (f)), were now cluttered with denser nanoscale precipitates.

Detailed microstructural features at the disk periphery after 30 turns and 30 turns + PDA are presented in the TEM/STEM images in Fig. 4 (a–c) and (d-f), respectively. It is noted that the imaging plane is

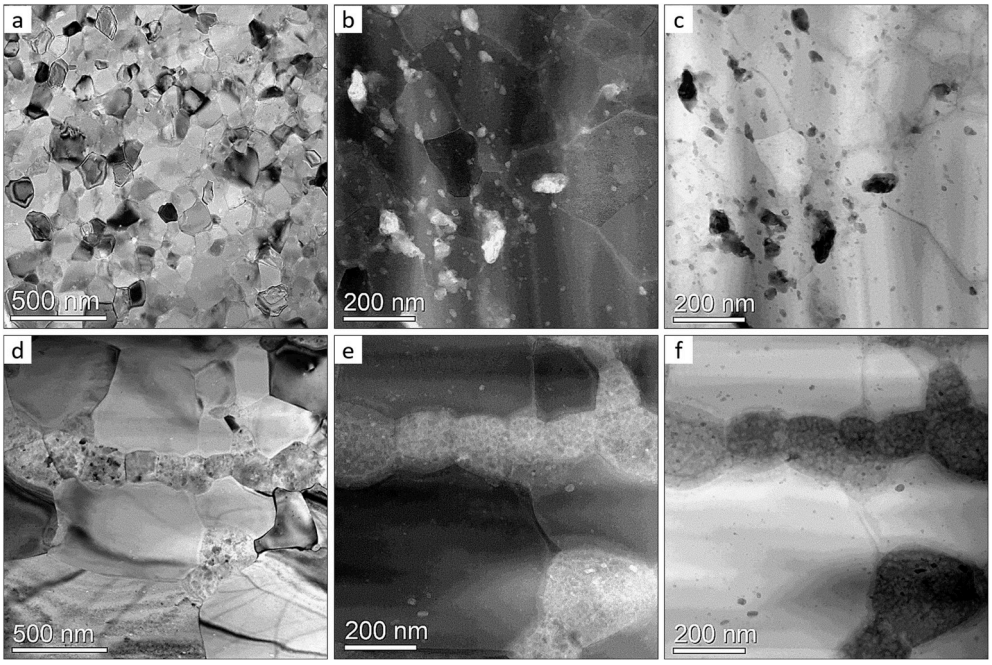

Fig. 4. Representative TEM/STEM images of the Zn–3Mg HPT hybrids at the periphery of the cross-section after 30 turns HPT: a) phase contrast TEM, b) BF-STEM, c) corresponding HAADF-STEM; and after 30 turns HPT + PDA (200 °C, 1 h): d) phase contrast TEM, e) BF-STEM, f) corresponding HAADF-STEM.

perpendicular to that of SEM images, as depicted in Fig. 1, such that the horizontal and vertical directions now correspond to the shear and thickness directions, respectively. The phase contrast TEM image in Fig. 4 (a) shows a reasonably equiaxed microstructure with grains of ~100–200 nm after 30 turns. This is in good agreement with the measurements taken from the SEM images, see Fig. 3 (c), suggesting that these nanoscale grains are equiaxed as a result of dynamic recrystallization during HPT. Fig. 4(b and c) show BF and corresponding HAADF STEM images after 30 turns, respectively. Numerous precipitates with a size distribution ranging between 20 and 150 nm, were randomly dispersed in the Zn-rich matrix, consistent with Fig. 3 (c). Furthermore, the darker appearance of these nanoprecipitates in the HAAD-STEM image suggests that they are richer in Mg than the Zn matrix.

The phase contrast TEM image in Fig. 4 (d) reveals a heterogeneous microstructure after PDA, in which nanograins of ~100–200 nm are confined within a matrix of significantly larger grains (~600–900 nm). The BF and corresponding HAADF STEM images provided in Fig. 4(e–f), respectively, show that nanoscale precipitates clustered primarily inside Mg-rich grains, in contrast to their distribution throughout the microstructure before PDA, see Fig. 3 (c). It is also noted that precipitate-rich grains generally exhibited finer dimensions than those of the precipitate-free Zn matrix. This suggests that the segregation of nanoprecipitates after PDA is assisted by diffusion, and that they act as obstacles to grain growth and stabilize Mg-rich grains.

3.2. In-situ phase transformation during HPT

XRD analysis was performed at the mid-thickness planes of the Zn–3Mg HPT hybrids after 1 turn, 15 turns, 30 turns, and 30 turns + PDA, and the results are shown in Fig. 5. Note that the intensity of the four scans was normalized to allow their comparison, and that the square root of the intensity was plotted in the vertical axis to better resolve low intensity peaks. Four different phases were identified and labeled accordingly: Zn (circle), Mg (diamond), Mg_2Zn_{11} (upside down triangle) and $MgZn_2$ (star). It is apparent from Fig. 5 that the sample after 1 turn consisted only of Zn and Mg, and the Mg peaks generally exhibited lower intensity than the Zn peaks, which is in agreement with the bulk composition. In contrast, after 15 and 30 turns, peaks corresponding to the intermetallic compounds Mg_2Zn_{11} and $MgZn_2$ were also identified. Moreover, it is evident from both the peak intensities and the presence of new peaks that the intermetallic phase amounts increase to some extent from 15 to 30 turns. Similarly, the Mg peaks generally either decrease their intensity or disappear through 30 turns.

This suggests that the deformation-enhanced atomic diffusion during HPT promotes the in-situ phase transformation from Mg to Mg_2Zn_{11} and $MgZn_2$. After 30 turns followed by PDA, it is observed that those peaks corresponding to Mg_2Zn_{11} tend to increase their intensity, whereas those associated with $MgZn_2$ show relatively low intensity after HPT. The composition of Mg_2Zn_{11} is 84.6Zn – 15.4Mg (at. %), whereas that of $MgZn_2$ is 67.5Zn – 32.5Mg (at. %), which implies that $MgZn_2$ requires about twice the amount of Mg atoms as Mg_2Zn_{11}. In addition, the formation enthalpy of $MgZn_2$, $\Delta H^{eq}_{MgZn_2} \sim -13.8$ kJ/mol, is greater than that of Mg_2Zn_{11}, $\Delta H^{eq}_{Mg_2Zn_{11}} \sim -8.96$ kJ/mol at 298 K [37]. Thereby, it is suggested that additional thermal activation during PDA promotes the decomposition of solute Mg atoms from $MgZn_2$ to Mg_2Zn_{11} by providing a lower energy to the hybrid system.

The presence of these two intermetallic compounds in the Mg-rich regions after PDA was confirmed through Fast Fourier Transform (FFT) analysis of the HRTEM images, as observed in Fig. 6. Two different regions of interest were investigated, see Fig. 6 (a and c), and their corresponding FFT diffractograms are presented in Fig. 6 (b and d), respectively. Reflections corresponding to Mg, $MgZn_2$ and Mg_2Zn_{11} were identified and labeled consistently, and their associated zone axes (ZA) are also presented.

3.3. Effect of PDA in the micro-mechanical behavior

The plastic behavior of the HPT hybrids was examined at the disk peripheries through a series of nanoindentation tests at four different CSR values. Fig. 7 shows representative load-displacement curves at $\dot{\varepsilon} = 1.25{\cdot}10^{-4}$, $2.5{\cdot}10^{-4}$, $5.0{\cdot}10^{-4}$, and $1.0{\cdot}10^{-3}$ s^{-1} after (a) 30 turns, and (b) 30 turns + PDA (200 °C, 1 h). It is apparent for both samples that there is some broadening between separate measurements under the same testing conditions, thereby reflecting a range of local micro-mechanical responses associated with the complex heterogeneous microstructures. These deviations in the plastic behavior indicates that a regime of plastic instability exists during deformation, and this is true

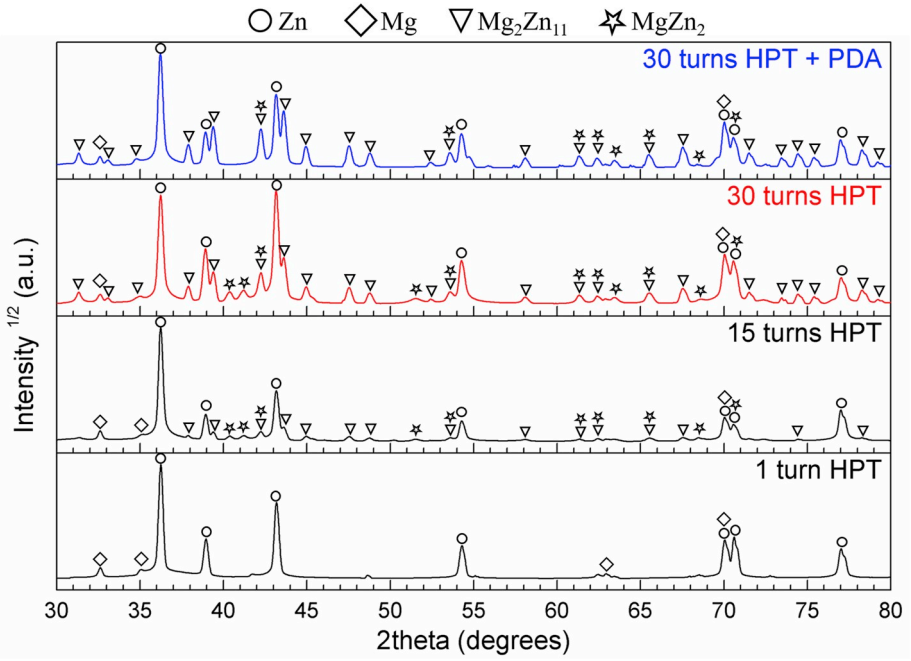

Fig. 5. X-ray diffraction profiles at the mid-thickness plane of the Zn–3Mg HPT hybrids after 1 turn, 15 turns, 30 turns, and 30 turns + PDA (200 °C, 1 h).

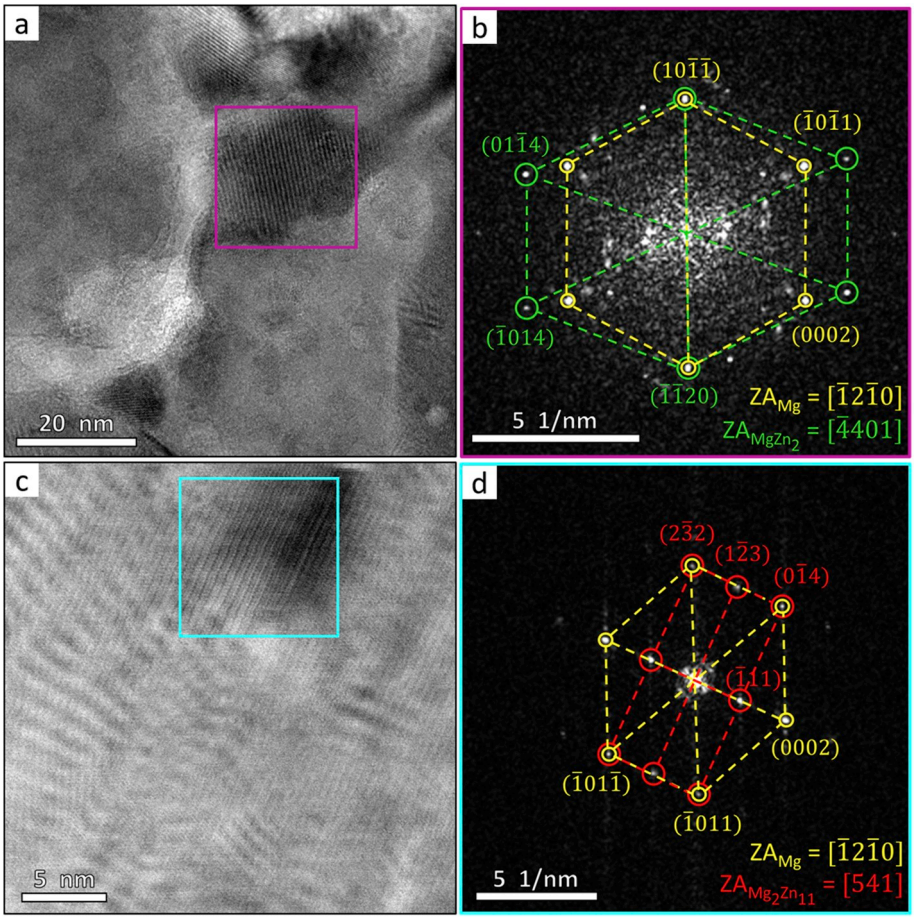

Fig. 6. HRTEM images of the Zn–3Mg HPT hybrid after PDA (a, c) and corresponding FFT diffractograms of the ROI highlighted in magenta and blue, respectively (b, d). Reflection planes of Mg (yellow), MgZn2 (green) and Mg2Zn11 (red), and their corresponding zone axes (ZA) are given. (For interpretation of the references to color in this figure legend, the reader is referred to the Web version of this article.)

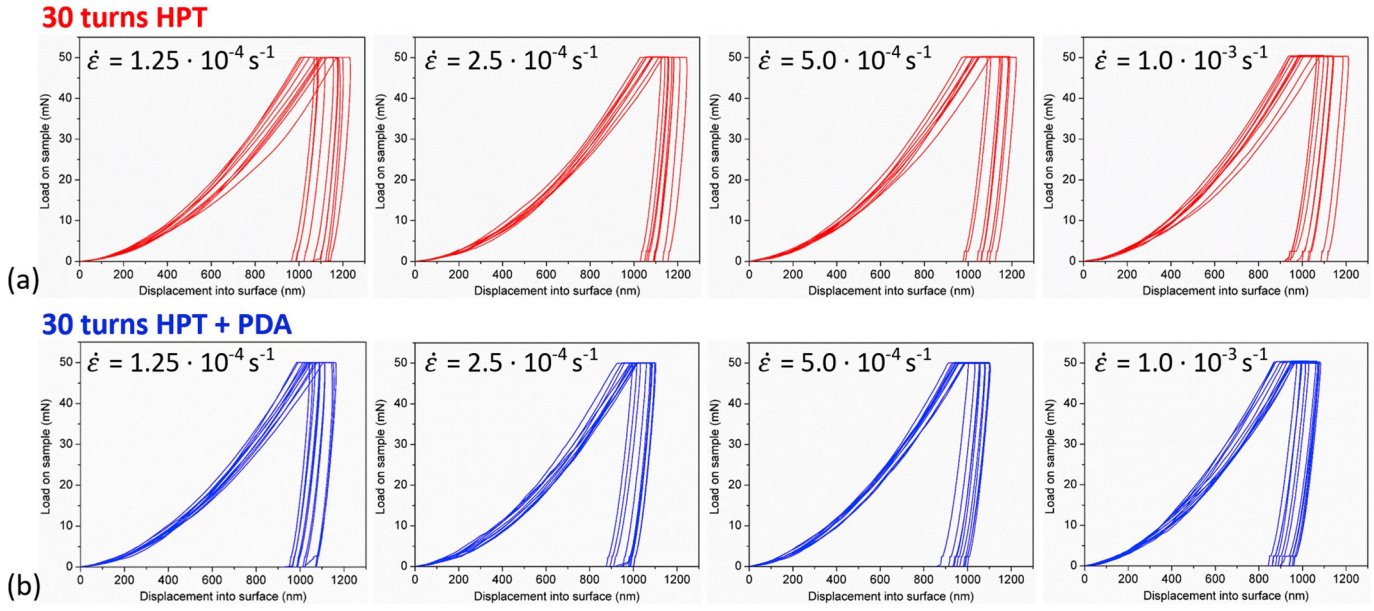

Fig. 7. Representative load-displacement curves of the Zn–3Mg hybrids from nanoindentation testing at constant strain rates $\dot{\varepsilon} = 1.25{\cdot}10^{-4}$, $2.5{\cdot}10^{-4}$, $5.0{\cdot}10^{-4}$, and $1.0{\cdot}10^{-3}\,s^{-1}$ at the disk periphery after (a) 30 turns HPT, and (b) 30 turns HPT + PDA (200 °C, 1 h).

for all strain rates tested. Thus, this instability is due to the coexistence of grains and intermetallic compounds with varying sizes, morphologies and distributions, which may lead to large strain gradients across the microstructure. Comparison of the load-displacement curves between the two material conditions at the same strain rates revealed that the sample which underwent PDA exhibited lower displacements in all cases. From this, it is inferred that this hybrid system becomes slightly harder upon PDA, which is consistent with the hardness measurements shown in Fig. 2 (b). Detailed inspection of the load-displacement curves at varying strain rates for each sample disclosed that the mean displacement at peak load decreases with increasing strain rate. This agrees with the general trend for metallic materials tested at faster strain rates to exhibit smaller indentation displacements, and thus, lower plasticity.

The strain rate dependence during plastic deformation was evaluated through the strain rate sensitivity, m, which was calculated from the nanoindentation dataset presented in Fig. 7, using Equation (2). The value of m was obtained from the slope of the linear fitting ($R^2 > 0.9$) in a logarithmic plot of $H/3$ vs. $\dot{\varepsilon}$, as shown in Fig. 8. The error bars represent their individual standard deviations, which are a result of the plastic instability evident in their corresponding load-displacement curves. Table 1 shows the numerical values of H for each $\dot{\varepsilon}$ and sample condition represented in Fig. 8. The m values were estimated as 0.098 after 30 turns HPT, and as 0.121 after 30 turns HPT + PDA. Thus, both m and H values increased consistently after PDA.

The value of V^* was estimated, using Equation (3), from the slope of the linear fit of logarithmic strain rate vs. linear flow stress. The calculated values of V^* for the Zn–3Mg HPT hybrid after 30 turns before and after PDA were $\sim 2.25\boldsymbol{b}^3$ and $\sim 1.35\boldsymbol{b}^3$, respectively, where $\boldsymbol{b} = 2.67{\cdot}10^{-10}$ m is the Burgers vector for Zn, and therefore, they are reasonably close to $\sim \boldsymbol{b}^3$. This suggests that grain boundary and/or lattice diffusion as well as surface diffusion are the dominant plastic deformation mechanisms for both the HPT and HPT + PDA samples [38]. Moreover, the value of V^* describes the plastic volume that is involved during plastic deformation, which is slightly larger after HPT than after HPT + PDA. This is in agreement with the larger values of displacement at peak load observed after 30 turns HPT in the load vs. displacement nanoindentation curves shown in Fig. 7.

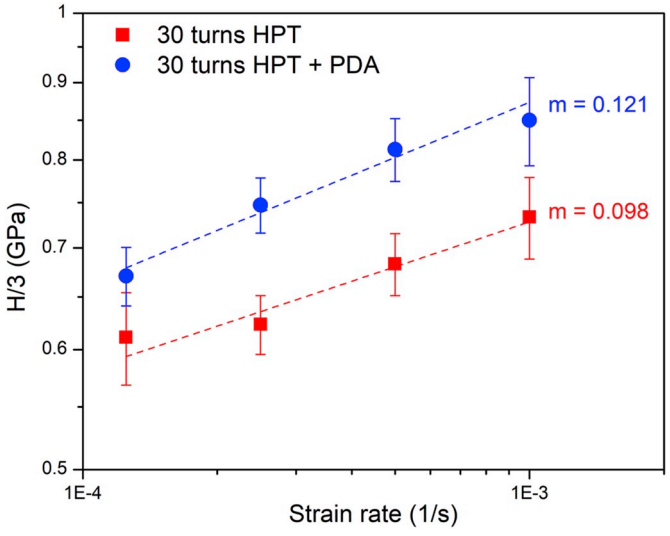

Fig. 8. Variation of the strain rate sensitivity, m, with increasing strain rate in the Zn–3Mg hybrids at the disk periphery after a) 30 turns HPT, and b) 30 turns HPT + PDA (200 °C, 1 h).

Table 1
Nanoindentation hardness, H, values represented in Fig. 8.

	30 turns HPT	30 turns HPT + PDA
$\dot{\varepsilon}$ (s^{-1})	H (GPa)	H (GPa)
$1.25{\cdot}10^{-4}$	1.834 ± 0.129	2.012 ± 0.089
$2.50{\cdot}10^{-4}$	1.870 ± 0.083	2.242 ± 0.094
$5.00{\cdot}10^{-4}$	2.050 ± 0.096	2.440 ± 0.116
$1.00{\cdot}10^{-3}$	2.201 ± 0.136	2.550 ± 0.170

4. Discussion

4.1. Unique microstructural formation in the HPT-processed hybrids and effect of PDA

HPT processing has been used to obtain hybrid materials through direct diffusion bonding of dissimilar bulk metals at RT, including Al-Cu [13,14], Al-Mg [15,16], Al-Fe [17], Al-Ti [17], Cu-Ta [18] and Zn–Mg [19]. These hybrids have generally shown good sample consolidation (i.e. without presence of voids or cracks) through deformation-induced solid-state reactions. Increasing the number of turns during HPT promotes the intermixing between different elements and leads to extensive grain refinement, particularly closer to the disk periphery where the plastic deformation is the largest. Moreover, some hybrid systems, like Al-Cu [13,14], Al-Mg [15,16] and Zn–Mg [19], exhibit in-situ precipitation of nanoscale intermetallic compounds during HPT, leading to a notable increase of the hardness values. However, the metal systems mentioned above presented non-homogeneous microstructures with a corresponding wide distribution of hardness levels across the disk diameter. In this work, the composition of the Zn–Mg HPT hybrids contained only 3Mg (wt. %), as opposed to the 10Mg (wt. %) studied previously [19]. This compositional change resulted in an enhanced microstructural homogeneity after 30 turns, see Fig. 2 (a). Consequently, this led to a more homogeneous hardness distribution across the sample, see Fig. 2 (b).

The effect of PDA on HPT-processed hybrids was first investigated in the Al–Mg system after 20 turns [15,16]. PDA led to a decrease of the hardness levels from ~330 HV to ~220 HV, and an enhanced plastic behavior evidenced by an increase of m from ~0 to ~0.1 in the Al–Mg system. Here, it is demonstrated that imposing a PDA treatment in Zn–3Mg HPT hybrids after 30 turns was effective in increasing both the H and m values simultaneously, suggesting an improved strength-ductility relationship. In general, this dual enhancement of the hardness and the plastic deformation capability is contrary to what has been reported in most HPT-processed materials having relatively homogeneous microstructures upon PDA [39–42]. It should be noted that the characterization of microstructural features in the Zn–3Mg hybrids after 30 turns was consistent with the SEM and TEM/STEM analysis performed on the perpendicular planes. This suggested that a fairly homogenous microstructure was achieved after HPT. However, upon subsequent PDA, preferential grain growth and segregation of nano-precipitates disrupted this homogeneity. In the same manner, materials exhibiting microstructural heterogeneity, including gradient structures [43], lamella structures [44] and harmonic structures [45], have recently shown a superior strain hardening capability, often related with a good combination of strength and ε_f. Their common feature with the Zn–3Mg HPT hybrids after PDA is that their microstructures consist of different domains, i.e. size, geometry or composition. These heterogeneities inherently possess notable strength differences, which will induce large strain gradients during severe plastic deformation. Therefore, the combined action of HPT and PDA in Zn–3Mg hybrids demonstrated a simultaneous enhancement of both H and m.

4.2. Synergistic effect of PDA on the micro-mechanical response of Zn–Mg HPT hybrids

In order to understand the influence of PDA in the load-displacement response of Zn–Mg HPT-processed hybrids, the unloading stiffness (S) and the displacement at peak load (h_{max}) were investigated from the CSR nanoindentation tests. The unloading stiffness is defined as the initial slope of the unloading curve at maximum load. The values of S and h_{max} were calculated for each individual curve shown in Fig. 7, and the average values are presented in Fig. 9(a) and (b), respectively, with their corresponding standard deviations indicated by the error bars. It should be noted that the upper portion of the unloading curve, in the range of 30–50 mN, was used for linear fitting of S. It is demonstrated that the values of both S and h_{max} decrease after PDA, as compared to immediately after HPT for 30 turns for the same strain rates. Moreover, S and h_{max} were also found to decrease with increasing strain rate in each sample condition. These observations are in good agreement with the positive m values reported in Fig. 8, as both S and h_{max} are inversely proportional to H [46]. The individual effect of S and h_{max} in the load-displacement behavior during nanoindentation is schematically represented in Fig. 9(c) and (d), respectively. It is observed that when $S_1 < S_2$, material 1 experiences larger elastic recovery, thus, exhibiting less plastic deformation, and consequently it is harder than material 2. Similarly, when $h_{max1} < h_{max2}$, material 1 requires less plastic strain to reach the peak load, and consequently it is harder than material 2.

It is proposed that the reason why the material after PDA exhibits both higher H and m values than after HPT processing is related to its heterogeneous microstructure [8,47]. This synergistic effect is suggested to be due to the presence of hard and soft domains playing complementary roles during deformation. Precipitate-free Zn-rich matrix grains are associated to the soft domains, whereas the ultrafine Mg-rich grains containing intermetallic nanoprecipitates correspond to the hard domains. Thereby, both domains will deform elastically during the first stage of deformation. Initial plastic deformation will be accommodated through dislocation slip on soft domains, while the hard domains remain elastic. This will create a mechanical incompatibility as the strain is no longer continuous across the microstructure, resulting in a plastic strain gradient in the soft domains. This strain gradient will be then accommodated by geometrically necessary dislocations (GNDs), which will pile-up at the domain interface leading to a back-stress that will strengthen the originally soft phase. Increasing plastic deformation will be accommodated by both hard and soft domains, and strain gradients are expected to exist near the domain boundaries. This will lead to the so-called strain partitioning [48–50], with neighboring domains sustaining different plastic strains and thus producing back-stress strengthening responsible for an enhanced strain hardening capability.

4.3. Exceptional strain hardening capability of Zn–Mg HPT hybrids

Earlier experiments have investigated the strain hardening behavior of metal alloys when processed by conventional HPT [51–53]. The degree of strain hardening was estimated through the hardenability exponent (η), which is given by the slope in a double-natural logarithm plot of the Vickers microhardness (HV) values against the equivalent strain (ε_{eq}) [51] where the estimation of equivalent strain during torsion straining is defined elsewhere [11]. The same approach was followed to evaluate the strain hardening capability of the Zn–3Mg HPT hybrids up to 30 turns, which is shown in Fig. 10 (a). Three distinct regimes can be observed in Fig. 10 (b). Regime I, $0 < \ln(\varepsilon_{eq}) < 3.5$, equivalent to strains of 1–30. Regime II, $3.5 < \ln(\varepsilon_{eq}) < 6.0$, equivalent to strains of ~30–400. Regime III, $6.0 < \ln(\varepsilon_{eq}) < 6.5$, equivalent to strains of ~400–660. Linear fitting of the experimental data within each of these regimes, revealed η values of 0.017, 0.535 and −0.668 for Regime I, II and III, respectively. Regime I indicated limited strain hardening in the early stage of HPT, as compared to HPT-processed Ti–6Al–4V ($\eta = 0.031$) [51], ZK60 ($\eta = 0.07$) [53], AZ31 ($\eta = 0.08$) [52]. It is noted that in these three alloys the hardness values saturate at $\ln(\varepsilon_{eq}) \approx 3$ during HPT processing. However, as observed in Regime II, the Zn–3Mg HPT hybrids do not reach hardness saturation in this range, but instead exhibit a significant increase of the strain hardening capability, with a hardenability exponent of $\eta = 0.535$. This value is about one order of magnitude higher than most reported values, and also the highest η value reported to date to the authors' knowledge, followed by HPT-processed high-purity Al with $\eta = 0.18$ [52].

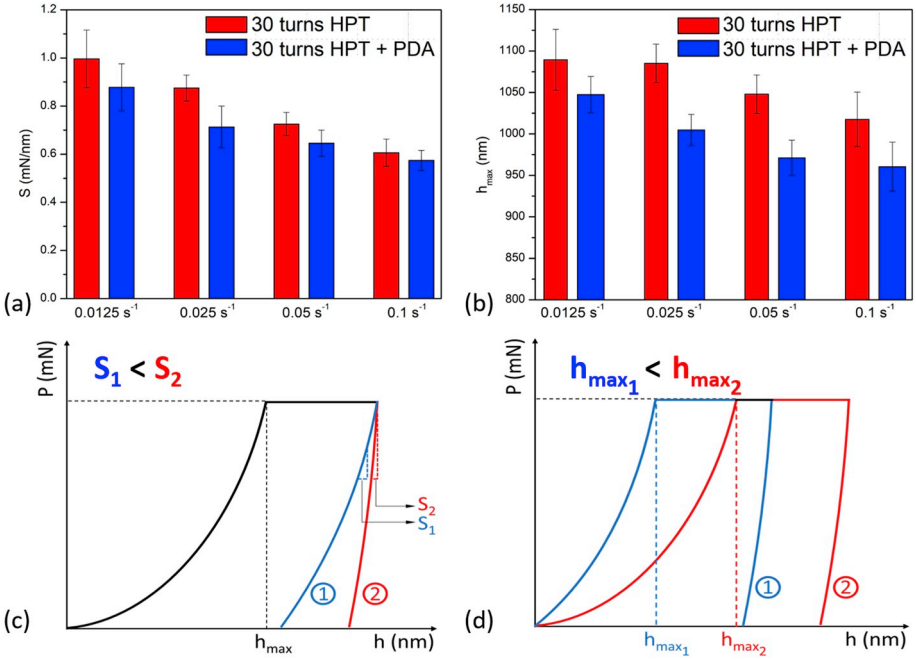

Fig. 9. Evolution of (a) unloading stiffness (S), and (b) maximum displacement into surface (h_{max}) at increasing strain rates during nanoindentation testing of Zn–3Mg hybrids at the disk periphery after 30 turns HPT and 30 turns HPT + PDA (200 °C, 1 h); Theoretical load-displacement responses of two materials having (c) different S values, and (d) different h_{max} values.

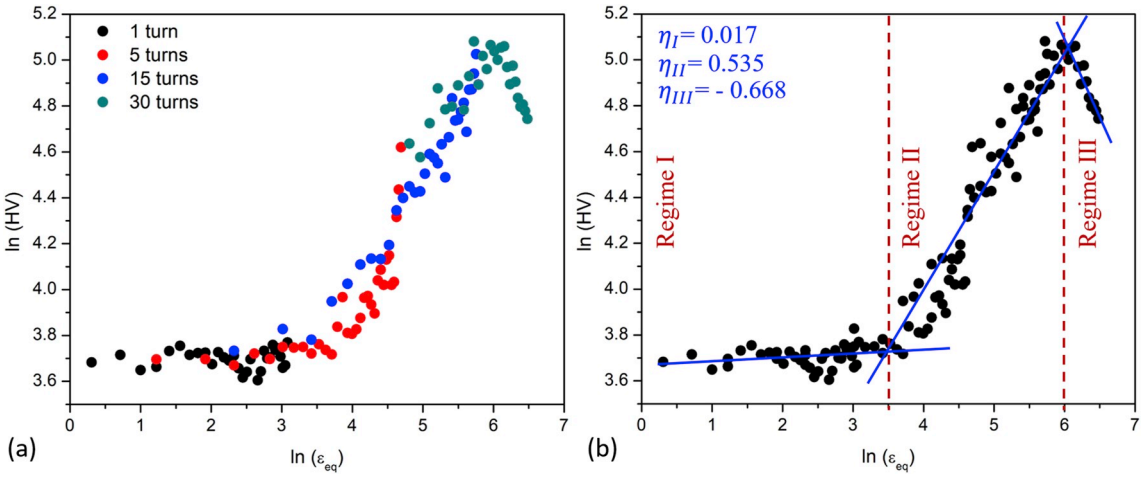

Fig. 10. Double-natural logarithm plots of hardness Vickers (HV) against equivalent strain (ε_{eq}) for the Zn–3Mg HPT hybrid (a) after 1, 5, 15 and 30 turns, and (b) determination of the hardenability exponent, η, in regimes I, II and III, delimited by red dash lines. Blue solid lines indicate the linear regressions. (For interpretation of the references to color in this figure legend, the reader is referred to the Web version of this article.)

This notable enhancement of the strain hardenability is suggested to be due to the contribution of multiple strengthening mechanisms, including severe grain refinement, in-situ precipitation of intermetallic compounds, and back-stress strengthening due to GNDs during HPT processing. At $\ln(\varepsilon_{eq}) \sim 6$, which is equivalent to $\varepsilon_{eq} \sim 400$, the Zn–3Mg HPT hybrids achieved the highest hardness, demonstrating a notable increase in the strain hardening capacity as compared to HPT-processed alloys [51–53]. Although there is a microstructural homogeneity in the Zn–Mg system after HPT for 30 turns, Regime III shows that additional plastic strain results in strain softening without hardness saturation, as indicated by a $\eta < 0$ value. This weakening behavior was also reported upon saturation in HPT-processed high-purity Al [52]. Moreover, it was found that the ratio between the hardening and softening exponent was −0.80 for the Zn–3Mg HPT hybrid, similar to −0.75 for the HPT-processed high-purity Al [52].

As was well defined in an earlier review on hardness behavior on HPT-processed materials [54], most pure metals and alloys can be classified into either of these three models: strain hardening, strain softening, or strain weakening during HPT. It should be noted that strain softening was also observed in high purity Zn [55] and Mg [56]. These different hardness behaviors occur due to the different rates of microstructural recovery and grain growth at the processing temperature. Because HPT is usually conducted at RT, the homologous temperature at RT (298 K) is used to define these three different models, thus $T_m/298$ [54].

The observed strain hardening in Region II in the present Zn–Mg hybrids after HPT for 30 turns is mainly attributed to the in-situ phase transformation of Mg to the $MgZn_2$ and Mg_2Zn_{11} intermetallic compounds, as shown in Fig. 5. An earlier report observed that the nanoindentation hardness of these two intermetallic compounds, formed by diffusion coupling, are ~5.08 GPa for $MgZn_2$ and ~3.76 GPa for Mg_2Zn_{11}, which are significantly higher than 0.54 GPa for Mg and 0.80 GPa for Zn [57]. Thus, increasing the numbers of HPT turns from 15 to 30 results in exceptional strain hardening due to the formation of these hard intermetallic nanoprecipitates. Thereafter, hardness softening follows in Region III, which may be due to the saturation of grain size refinement after severe straining, as shown in Fig. 2 (a). Such nanostructures hold a large volume fraction of high-angle grain boundaries which can activate the grain boundary sliding at ambient temperature [58] leading to the high strain rate sensitivity observed at the disk edge of the Zn–Mg hybrid after 30 turns, as shown in Fig. 8. Thus, the transition between Region II and III demonstrates a clear tradeoff of the hardness-plasticity relationship in HPT hybrids. Although there is no direct measurement of the ε_f in the present study, it is well established that there is a correlation between ε_f and strain rate sensitivity [59]. Thus, the enhancement in both strain hardening and the strain rate sensitivity due to the unique heterostructure synthesized by HPT suggests an enhanced strength-ductility combination of the HPT-processed Zn–Mg hybrids.

5. Summary and conclusions

1. Zn–3Mg (wt. %) hybrids were synthesized using quasi-constrained HPT processing under 6 GPa and 1 rpm for 1, 5, 15 and 30 turns for a series of Zn/Mg/Zn disks. The microstructural and hardness evolution during HPT and subsequent PDA (200 °C, 1 h) was investigated by SEM, XRD, TEM/STEM, Vickers hardness and nanoindentation testing.
2. A relatively homogenous microstructure, consisting of ultrafine equiaxed grains (~100–200 nm in diameter) and nanoscale precipitates evenly distributed, was achieved at the disk periphery after 30 turns. The Vickers hardness followed a symmetric gradient-type evolution with respect to the center from 1 to 30 turns, having maximum values within the range of 200–230 HV.
3. PDA after 30 turns led to a significant microstructural heterogeneity, consisting of a bimodal grain size distribution of ~100–200 nm and ~600–900 nm. This was suggested as a result of segregation of nanoprecipitates in Mg-rich grains, which may act as pinning sites preventing grain growth during annealing. The HPT hybrids did not exhibited softening after PDA, but instead presented maximum Vickers hardness values in the range of 210–250 HV.
4. In-situ precipitation of $MgZn_2$ and Mg_2Zn_{11} intermetallic compounds during HPT was revealed through XRD after 15 turns, and their volume fraction increased after 30 turns. Subsequent PDA resulted in an increase of the Mg_2Zn_{11} vol fraction at the expense of $MgZn_2$, which was suggested due to a decrease in the formation enthalpy, providing a lower energy state for the HPT hybrid system. FFT analysis confirmed the presence of Mg_2Zn_{11} and $MgZn_2$ intermetallics within Mg-rich regions after PDA.
5. Nanoindentation testing concluded that both H and m values increased after PDA. The H values increased consistently with strain rate in both material conditions, indicating lower plasticity at faster strain rates. The m values were estimated as 0.098 and 0.121, before and after PDA, respectively. This demonstrated that PDA was able to provide a dual enhancement of hardness and plastic deformation capability, contrary to the classical strength-ductility tradeoff.
6. Close inspection of the strain hardening capability revealed that Zn–Mg HPT hybrids follow a three-regime behavior during

deformation. Regime I, up to ε_{eq} ~30, indicated a limited strain hardening in the early stage of HPT, with a hardenability exponent of $\eta = 0.017$. Regime II, up to ε_{eq} ~400, showed an exceptional strain hardening, with $\eta = 0.535$, which is about one order of magnitude larger than most reported values. Regime III, up to ε_{eq} ~660, exhibited softening, which may be due to the saturation of the grain size refinement after severe straining. Transition between Regime II and III demonstrated a clear tradeoff in the hardness-plasticity relationship.

7. These results confirmed that PDA has a synergistic effect on the micro-mechanical behavior of Zn–Mg hybrids processed by HPT. Although there was no direct measurement of the ε_f in the present study, the proven enhancement in both strain hardening and strain rate sensitivity suggested that the unique heterostructure synthesized by HPT + PDA may exhibit an excellent strength-ε_f combination. This could not only make Zn–Mg hybrids attractive for absorbable medical applications, but also inspire researchers towards the design of heterostructure materials with enhanced properties for task-specific applications.

Data availability

The raw/processed data required to reproduce these findings cannot be shared at this time as the data also forms part of an ongoing study.

Declaration of competing interest

The authors declare that they have no known competing financial interests or personal relationships that could have appeared to influence the work reported in this paper.

Acknowledgements

The funding for this research was supported by the National Science Foundation Division of Materials Research, under Grant No. DMR-1607942 through the Metals and Metallic Nanostructures (MMN) program (DHE & CJB), and under Grant No. DMR-1810343 (JKH & MK). A portion of this research (TEM/STEM) was conducted at Oak Ridge National Laboratory's Center for Nanophase Materials Sciences, a U.S. Department of Energy Office of Science User Facility.

References

[1] F. Witte, The history of biodegradable magnesium implants: a review, Acta Biomater. 23 (2015) S28–S40, https://doi.org/10.1016/j.actbio.2015.07.017.
[2] M. Peuster, C. Hesse, T. Schloo, C. Fink, P. Beerbaum, C. von Schnakenburg, Long-term biocompatibility of a corrodible peripheral iron stent in the porcine descending aorta, Biomaterials 27 (2006) 4955–4962, https://doi.org/10.1016/j.biomaterials.2006.05.029.
[3] P.K. Bowen, J. Drelich, J. Goldman, Zinc exhibits ideal physiological corrosion behavior for bioabsorbable stents, Adv. Mater. (2013), https://doi.org/10.1002/adma.201300226.
[4] P.K. Bowen, R.J. Guillory, E.R. Shearier, J.M. Seitz, J. Drelich, M. Bocks, F. Zhao, J. Goldman, Metallic zinc exhibits optimal biocompatibility for bioabsorbable endovascular stents, Mater. Sci. Eng. C (2015), https://doi.org/10.1016/j.msec.2015.07.022.
[5] H. Yang, C. Wang, C. Liu, H. Chen, Y. Wu, J. Han, Z. Jia, W. Lin, D. Zhang, W. Li, W. Yuan, H. Guo, H. Li, G. Yang, D. Kong, D. Zhu, K. Takashima, L. Ruan, J. Nie, X. Li, Y. Zheng, Evolution of the degradation mechanism of pure zinc stent in the one-year study of rabbit abdominal aorta model, Biomaterials 145 (2017) 92–105, https://doi.org/10.1016/j.biomaterials.2017.08.022.
[6] C. Xiao, L. Wang, Y. Ren, S. Sun, E. Zhang, C. Yan, Q. Liu, X. Sun, F. Shou, J. Duan, H. Wang, G. Qin, Indirectly extruded biodegradable Zn-0.05wt%Mg alloy with improved strength and ductility: in vitro and in vivo studies, J. Mater. Sci. Technol. (2018), https://doi.org/10.1016/J.JMST.2018.01.006.
[7] E. Mostaed, M. Sikora-Jasinska, A. Mostaed, S. Loffredo, A.G. Demir, B. Previtali, D. Mantovani, R. Beanland, M. Vedani, Novel Zn-based alloys for biodegradable stent applications: design, development and in vitro degradation, J. Mech. Behav. Biomed. Mater. (2016), https://doi.org/10.1016/j.jmbbm.2016.03.018.
[8] E. Ma, T. Zhu, Towards strength–ductility synergy through the design of heterogeneous nanostructures in metals, Mater. Today 20 (2017) 323–331, https://doi.org/10.1016/J.MATTOD.2017.02.003.
[9] Y. Wang, M. Chen, F. Zhou, E. Ma, High tensile ductility in a nanostructured metal, Nature 419 (2002) 912–915, https://doi.org/10.1038/nature01133.
[10] L. Wang, Y. Shi, Y. Zhang, M. Li, High tensile ductility and strength in a gradient structured Zr, Mater. Lett. 228 (2018) 500–503, https://doi.org/10.1016/J.MATLET.2018.06.084.
[11] A.P. Zhilyaev, T.G. Langdon, Using high-pressure torsion for metal processing: fundamentals and applications, Prog. Mater. Sci. 53 (2008) 893–979, https://doi.org/10.1016/j.pmatsci.2008.03.002.
[12] R. Kapoor, Severe plastic deformation of materials, in: Mater. Under Extrem. Cond., Elsevier, 2017, pp. 717–754, https://doi.org/10.1016/B978-0-12-801300-7.00020-6.
[13] K. Oh-ishi, K. Edalati, H.S. Kim, K. Hono, Z. Horita, High-pressure torsion for enhanced atomic diffusion and promoting solid-state reactions in the aluminum–copper system, Acta Mater. 61 (2013) 3482–3489, https://doi.org/10.1016/J.ACTAMAT.2013.02.042.
[14] J.-K. Han, D.K. Han, G.Y. Liang, J.-I. Jang, T.G. Langdon, M. Kawasaki, Direct bonding of aluminum-copper metals through high-pressure torsion processing, Adv. Eng. Mater. 20 (2018), https://doi.org/10.1002/adem.201800642, 1800642.
[15] M. Kawasaki, B. Ahn, H.-J. Lee, A.P. Zhilyaev, T.G. Langdon, Using high-pressure torsion to process an aluminum-magnesium nanocomposite through diffusion bonding, Acta Mater. 59 (2015) 1974–1985, https://doi.org/10.1016/j.actamat.2010.11.063.
[16] J.K. Han, H.J. Lee, J. il Jang, M. Kawasaki, T.G. Langdon, Micro-mechanical and tribological properties of aluminum-magnesium nanocomposites processed by high-pressure torsion, Mater. Sci. Eng. A 684 (2017) 318–327, https://doi.org/10.1016/j.msea.2016.12.067.
[17] M. Kawasaki, J.-K. Han, D.-H. Lee, J. Jang, T.G. Langdon, Fabrication of nanocomposites through diffusion bonding under high-pressure torsion, J. Mater. Res. (2018) 1–11, https://doi.org/10.1557/jmr.2018.205.
[18] N. Ibrahim, M. Peterlechner, F. Emeis, M. Wegner, S.V. Divinski, G. Wilde, Mechanical alloying via high-pressure torsion of the immiscible Cu50Ta50 system, Mater. Sci. Eng. A 685 (2017) 19–30, https://doi.org/10.1016/j.msea.2016.12.106.
[19] D. Hernández-Escobar, Z.U. Rahman, H. Yilmazer, M. Kawasaki, C.J. Boehlert, Microstructural evolution and intermetallic formation in Zn Mg hybrids processed by High Pressure Torsion, Philos. Mag. 99 (2019) 557–584, https://doi.org/10.1080/14786435.2018.1546962.
[20] G. Dunea, S.D. Mahurkar, B. Mamdani, E.C. Smith, Role of aluminum in dialysis dementia, Ann. Intern. Med. 88 (1978) 502–504, https://doi.org/10.7326/0003-4819-88-4-502.
[21] A. Mirza, A. King, C. Troakes, C. Exley, Aluminium in brain tissue in familial Alzheimer's disease, J. Trace Elem. Med. Biol. 40 (2017) 30–36, https://doi.org/10.1016/j.jtemb.2016.12.001.
[22] D. Hernández-Escobar, S. Champagne, H. Yilmazer, B. Dikici, C.J. Boehlert, H. Hermawan, Current status and perspectives of zinc-based absorbable alloys for biomedical applications, Acta Biomater. (2019), https://doi.org/10.1016/j.actbio.2019.07.034.
[23] R.Z. Valiev, I.V. Alexandrov, Y.T. Zhu, T.C. Lowe, Paradox of strength and ductility in metals processed by severe plastic deformation, J. Mater. Res. 17 (2002) 5–8, https://doi.org/10.1557/JMR.2002.0002.
[24] K. Edalati, Y. Hashiguchi, P.H.R. Pereira, Z. Horita, T.G. Langdon, Effect of temperature rise on microstructural evolution during high-pressure torsion, Mater. Sci. Eng. A 714 (2018) 167–171, https://doi.org/10.1016/j.msea.2017.12.095.
[25] B.N. Lucas, W.C. Oliver, Indentation Power-Law Creep of High-Purity Indium. https://link.springer.com/content/pdf/10.1007%2Fs11661-999-0051-7.pdf, 1999 accessed April 9, 2019.
[26] C.L. Wang, Y.H. Lai, J.C. Huang, T.G. Nieh, Creep of nanocrystalline nickel: a direct comparison between uniaxial and nanoindentation creep, Scr. Mater. 62 (2010) 175–178, https://doi.org/10.1016/j.scriptamat.2009.10.021.
[27] I.-C. Choi, B.-G. Yoo, Y.-J. Kim, M.-Y. Seok, Y. Wang, J. Jang, Estimating the stress exponent of nanocrystalline nickel: sharp vs. spherical indentation, Scr. Mater. 65 (2011) 300–303, https://doi.org/10.1016/J.SCRIPTAMAT.2011.04.031.
[28] W.C. Oliver, G.M. Pharr, An Improved Technique for Determining Hardness and Elastic Modulus Using Load and Displacement Sensing Indentation Experiments, 2018, https://doi.org/10.1557/JMR.1992.1564.
[29] S. Shim, J. Jang, G.M. Pharr, Extraction of flow properties of single-crystal silicon carbide by nanoindentation and finite-element simulation, Acta Mater. 56 (2008) 3824–3832, https://doi.org/10.1016/J.ACTAMAT.2008.04.013.
[30] Q. Wei, Strain rate effects in the ultrafine grain and nanocrystalline regimes—influence on some constitutive responses, J. Mater. Sci. 42 (2007) 1709–1727, https://doi.org/10.1007/s10853-006-0700-9.
[31] I. POSPÍŠILOVÁ, D. VOJTĚCH, Mechanical properties of Zn-Mg alloys, Metal 15 (2013) 15–17.
[32] S.-Y. Chang, S.-W. Lee, K.M. Kang, S. Kamado, Y. Kojima, Improvement of mechanical characteristics in severely plastic-deformed Mg alloys, Mater. Trans. 45 (2005) 488–492, https://doi.org/10.2320/matertrans.45.488.

[33] Y. Cao, M. Kawasaki, Y.B. Wang, S.N. Alhajeri, X.Z. Liao, W.L. Zheng, S.P. Ringer, Y.T. Zhu, T.G. Langdon, Unusual macroscopic shearing patterns observed in metals processed by high-pressure torsion, J. Mater. Sci. 45 (2010) 4545–4553, https://doi.org/10.1007/s10853-010-4485-5.
[34] Y. Cao, Y.B. Wang, R.B. Figueiredo, L. Chang, X.Z. Liao, M. Kawasaki, W.L. Zheng, S.P. Ringer, T.G. Langdon, Y.T. Zhu, Three-dimensional shear-strain patterns induced by high-pressure torsion and their impact on hardness evolution, Acta Mater. 59 (2011) 3903–3914, https://doi.org/10.1016/J.ACTAMAT.2011.03.015.
[35] Y. Huang, M. Kawasaki, T.G. Langdon, Influence of Anvil alignment on shearing patterns in high-pressure torsion, Adv. Eng. Mater. 15 (2013) 747–755, https://doi.org/10.1002/adem.201200363.
[36] R. Kulagin, Y. Beygelzimer, A. Bachmaier, R. Pippan, Y. Estrin, Benefits of pattern formation by severe plastic deformation, Appl. Mater. Today. 15 (2019) 236–241, https://doi.org/10.1016/J.APMT.2019.02.007.
[37] M. Morishita, H. Yamamoto, S. Shikada, M. Kusumoto, Y. Matsumoto, Thermodynamics of the formation of magnesium–zinc intermetallic compounds in the temperature range from absolute zero to high temperature, Acta Mater. 54 (2006) 3151–3159, https://doi.org/10.1016/J.ACTAMAT.2006.03.004.
[38] H. Frost, M. Ashby, Deformation mechanism maps: the plasticity and creep of metals and ceramics. http://publications.eng.cam.ac.uk/372960/, 1982 accessed May 19, 2019.
[39] Y. Huang, M. Lemang, N.X. Zhang, P.H.R. Pereira, T.G. Langdon, Achieving superior grain refinement and mechanical properties in vanadium through high-pressure torsion and subsequent short-term annealing, Mater. Sci. Eng. A 655 (2016) 60–69, https://doi.org/10.1016/J.MSEA.2015.12.086.
[40] O. Andreau, J. Gubicza, N. Xian Zhang, Y. Huang, P. Jenei, T.G. Langdon, Effect of short-term annealing on the microstructures and flow properties of an Al-1% Mg alloy processed by high-pressure torsion, Mater. Sci. Eng. A 615 (2014) 231–239, https://doi.org/10.1016/j.msea.2014.07.018.
[41] H. Shahmir, J. He, Z. Lu, M. Kawasaki, T.G. Langdon, Effect of annealing on mechanical properties of a nanocrystalline CoCrFeNiMn high-entropy alloy processed by high-pressure torsion, Mater. Sci. Eng. A 676 (2016) 294–303, https://doi.org/10.1016/J.MSEA.2016.08.118.
[42] P. Sathiyamoorthi, J. Bae, P. Asghari-Rad, J. Park, J. Kim, H. Kim, P. Sathiyamoorthi, J.W. Bae, P. Asghari-Rad, J.M. Park, J.G. Kim, H.S. Kim, Effect of annealing on microstructure and tensile behavior of CoCrNi medium entropy alloy processed by high-pressure torsion, Entropy 20 (2018) 849, https://doi.org/10.3390/e20110849.
[43] X. Wu, P. Jiang, L. Chen, F. Yuan, Y.T. Zhu, Extraordinary strain hardening by gradient structure, Proc. Natl. Acad. Sci. 111 (2014) 7197–7201, https://doi.org/10.1073/PNAS.1324069111.
[44] X. Wu, M. Yang, F. Yuan, G. Wu, Y. Wei, X. Huang, Y. Zhu, Heterogeneous lamella structure unites ultrafine-grain strength with coarse-grain ductility, Proc. Natl. Acad. Sci. U. S. A 112 (2015) 14501–14505, https://doi.org/10.1073/pnas.1517193112.
[45] D. Orlov, H. Fujiwara, K. Ameyama, Obtaining copper with harmonic structure for the optimal balance of structure-performance relationship, Mater. Trans. 54 (2013) 1549–1553, https://doi.org/10.2320/matertrans.mh201320.
[46] C. Charitidis, Nanomechanical properties and nanoscale deformation of engineering metals and alloys, in: Mater. Surf. Eng., Elsevier, 2012, pp. 23–59, https://doi.org/10.1533/9780857096036.23.
[47] X. Wu, Y. Zhu, Heterogeneous Materials: a New Class of Materials with Unprecedented Mechanical Properties, vol. 5, 2017, pp. 527–532, https://doi.org/10.1080/21663831.2017.1343208.
[48] Z.H. Cong, N. Jia, X. Sun, Y. Ren, J. Almer, Y.D. Wang, Stress and strain partitioning of ferrite and martensite during deformation, Metall. Mater. Trans. A 40 (2009) 1383–1387, https://doi.org/10.1007/s11661-009-9824-2.
[49] Q. Han, A. Asgari, P.D. Hodgson, N. Stanford, Strain partitioning in dual-phase steels containing tempered martensite, Mater. Sci. Eng. A 611 (2014) 90–99, https://doi.org/10.1016/J.MSEA.2014.05.078.
[50] M.-M. Wang, C.C. Tasan, D. Ponge, A.-C. Dippel, D. Raabe, Nanolaminate transformation-induced plasticity–twinning-induced plasticity steel with dynamic strain partitioning and enhanced damage resistance, Acta Mater. 85 (2015) 216–228, https://doi.org/10.1016/J.ACTAMAT.2014.11.010.
[51] Y.C. Wang, T.G. Langdon, Effect of heat treatment on microstructure and microhardness evolution in a Ti–6Al–4V alloy processed by high-pressure torsion, J. Mater. Sci. 48 (2013) 4646–4652, https://doi.org/10.1007/s10853-012-7071-1.
[52] M. Kawasaki, R.B. Figueiredo, Y. Huang, T.G. Langdon, Interpretation of hardness evolution in metals processed by high-pressure torsion, J. Mater. Sci. 49 (2014) 6586–6596, https://doi.org/10.1007/s10853-014-8262-8.
[53] S.A. Torbati-Sarraf, S. Sabbaghianrad, R.B. Figueiredo, T.G. Langdon, Orientation imaging microscopy and microhardness in a ZK60 magnesium alloy processed by high-pressure torsion, J. Alloy. Comp. 712 (2017) 185–193, https://doi.org/10.1016/J.JALLCOM.2017.04.054.
[54] M. Kawasaki, Different models of hardness evolution in ultrafine-grained materials processed by high-pressure torsion, J. Mater. Sci. 49 (2014) 18–34, https://doi.org/10.1007/s10853-013-7687-9.
[55] K. Edalati, Z. Horita, Significance of homologous temperature in softening behavior and grain size of pure metals processed by high-pressure torsion, Mater. Sci. Eng. A 528 (2011) 7514–7523, https://doi.org/10.1016/j.msea.2011.06.080.
[56] K. Edalati, A. Yamamoto, Z. Horita, T. Ishihara, High-pressure torsion of pure magnesium: evolution of mechanical properties, microstructures and hydrogen storage capacity with equivalent strain, Scr. Mater. 64 (2011) 880–883, https://doi.org/10.1016/j.scriptamat.2011.01.023.
[57] C.C. Kammerer, S. Behdad, L. Zhou, F. Betancor, M. Gonzalez, B. Boesl, Y.H. Sohn, Diffusion kinetics, mechanical properties, and crystallographic characterization of intermetallic compounds in the Mg–Zn binary system, Intermetallics 67 (2015) 145–155, https://doi.org/10.1016/J.INTERMET.2015.08.001.
[58] N.Q. Chinh, T. Csanádi, J. Gubicza, R.Z. Valiev, B.B. Straumal, T.G. Langdon, The effect of grain boundary sliding and strain rate sensitivity on the ductility of ultrafine-grained materials, Mater. Sci. Forum 667–669 (2010) 677–682. https://doi.org/10.4028/www.scientific.net/MSF.667-669.677.
[59] D. Woodford, Strain-rate sensitivity as a measure of ductility, ASM Trans. Quart. 62 (1969).